

Cite this: *Phys. Chem. Chem. Phys.*,  
2014, 16, 3095

# Understanding improved electrochemical properties of NiO-doped NiF<sub>2</sub>-C composite conversion materials by X-ray absorption spectroscopy and pair distribution function analysis†

Dae Hoe Lee,<sup>a</sup> Kyler J. Carroll,<sup>a</sup> Karena W. Chapman,<sup>b</sup> Olaf J. Borkiewicz,<sup>b</sup> Scott Calvin,<sup>c</sup> Eric E. Fullerton<sup>a</sup> and Ying Shirley Meng<sup>\*a</sup>

The conversion reactions of pure NiF<sub>2</sub> and the NiO-doped NiF<sub>2</sub>-C composite (NiO-NiF<sub>2</sub>-C) were investigated using X-ray absorption spectroscopy (XAS) and pair distribution function (PDF) analysis. The enhanced electronic conductivity of NiO-NiF<sub>2</sub>-C is associated with a significant improvement in the reversibility of the conversion reaction compared to pure NiF<sub>2</sub>. Different evolutions of the size distributions of the Ni nanoparticles formed during discharge were observed. While a bimodal nanoparticle size distribution was maintained for NiO-NiF<sub>2</sub>-C following the 1st and 2nd discharge, for pure NiF<sub>2</sub> only smaller nanoparticles (~14 Å) remained following the 2nd discharge. We postulate that the solid electrolyte interphase formed upon the 1st discharge at large overpotential retards the growth of metallic Ni leading to formation of smaller Ni particles during the 2nd discharge. In contrast, the NiO doping and the carbon layer covering the NiO-NiF<sub>2</sub>-C possibly facilitate the conversion process on the surface preserving the reaction kinetics upon the 2nd discharge. Based on the electronic conductivity and surface properties, the resulting size of the Ni nanoparticles is associated with the conversion kinetics and consequently the cyclability.

Received 19th October 2013,  
Accepted 12th December 2013

DOI: 10.1039/c3cp54431a

www.rsc.org/pccp

## Introduction

Although the performance of Li-ion batteries has been improved dramatically in recent years, the limit in terms of the energy density still needs to be resolved to meet the growing demands for large-scale mobile devices (*e.g.*, electric vehicles) and minimizing the size of portable electronics. One way to achieve a greater energy density is to utilize multiple Li-ions per redox active metal center, on the contrary to the intercalation-based cathodes which can employ only 0.5–1.0 Li-ions. The limited capacity can be overcome by utilizing conversion-based cathodes that exhibit substantially greater capacities due to the fact that more than 2 Li-ions per 1 redox active metal can be utilized during the conversion reaction.<sup>1,2</sup> Since the inception of the high capacity reversible Li conversion reaction in transition metal (TM) oxides, there have been several different types of conversion materials studied over the years.<sup>3–9</sup> The issue with these materials is that

the thermodynamic potential for the conversion is low, which is not suitable for the cathode materials. Only TM fluorides, however, show a relatively high conversion potential due to high ionicity of the TM-F<sub>x</sub> bond.<sup>10</sup> As such, considerable effort has been devoted to tailoring the nanostructures to overcome their poor electronic conductivity. It has been demonstrated that nanocomposites of carbon and TM fluorides such as FeF<sub>2</sub>, FeF<sub>3</sub>, and BiF<sub>3</sub> may be utilized as cathodes for high energy Li-ion batteries, revealing a high conversion potential and acceptable cycling properties.<sup>11–16</sup> In addition, the TM fluoride compounds that include an M–O covalent bond such as FeOF and Fe<sub>2</sub>OFe<sub>4</sub> have been reported to exhibit better electrochemical properties in terms of the cyclability, since the M–O bond provides a higher electronic conductivity to the highly insulating M–F bond.<sup>17,18</sup>

Since the conversion process involves the metallic nanoparticles (NPs) embedded in an amorphous LiX (X = O or F) phase, it is difficult to analyze the structures utilizing standard crystallographic techniques. Therefore, many advanced techniques which are sensitive to both structure and chemistry have been utilized to understand underlying mechanisms and the electrochemical behavior.<sup>19–24</sup> The element-specific nature and high sensitivity to the local chemical environment of the XAS technique makes it an ideal tool to study the electronic structural properties and inter-atomic environment.<sup>25</sup> PDF analysis of total scattering provides an in-depth understanding of the

<sup>a</sup> Department of NanoEngineering, University of California San Diego, 9500 Gilman Drive, La Jolla, CA 92093, USA. E-mail: shirleymeng@ucsd.edu; Fax: +1-858-534-9553; Tel: +1-858-822-4247

<sup>b</sup> X-ray Science Division, Advanced Photon Source, Argonne National Laboratory, 9700 South Cass Avenue, Argonne, IL 60439, USA

<sup>c</sup> Department of Physics, Sarah Lawrence College, Bronxville, NY 10708, USA

† Electronic supplementary information (ESI) available. See DOI: 10.1039/c3cp54431a

inter-atomic structure, phase distribution, and particle size, independent of long-range order.<sup>26</sup> Recently, research by Wang *et al.* has demonstrated by TEM and PDF that the nanosized Fe particles (1–3 nm in diameter) are interconnected in the lithiated FeF<sub>2</sub> and form a bicontinuous network, which provides a pathway for local electron transport through the insulating LiF phase.<sup>20,21</sup> In addition to FeF<sub>2</sub>, isostructural oxide doped FeOF, which shows enhanced electrochemical performance, has been comprehensively studied using *in situ* PDF and NMR.<sup>27</sup> It was suggested that the preferential reaction of Fe in a F-rich phase, caused by anion partitioning of F-rich rutile and O-rich rock salt during the cycling, may result in improved electrochemical properties in this system.

A major effort thus far has focused on FeF<sub>x</sub>-based compounds due to their superior electrochemical properties, and investigated only upon the 1st cycle. However, there are only a very few reports on NiF<sub>2</sub> in terms of its conversion mechanisms and the electrochemical properties. Zhang *et al.* reported that the nanostructured NiF<sub>2</sub> thin film fabricated by pulsed laser deposition (PLD) displayed acceptable cycling until 40 cycles at the conversion potential of 0.7 V, much lower than theoretical potential.<sup>28</sup> In our previous work, pure NiF<sub>2</sub> showed poor electrochemical properties in terms of the cyclability and NiO doping into NiF<sub>2</sub> turned out to be beneficial to the reversibility.<sup>29</sup> The Ni NPs size was approximated to be smaller in the lithiated NiF<sub>2</sub> than NiO doped NiF<sub>2</sub> by magnetic measurements, but direct evidence of the Ni NPs dimensions and detailed phase distribution in the lithiated electrodes have yet to be reported.

NiF<sub>2</sub> is a rutile structure (*P4<sub>2</sub>/mnm*, *a* ~ 4.65 Å, *c* ~ 3.08 Å) with TM occupying the corners and the center of a tetragonal unit cell, and six fluorine atoms forming the quasi-octahedral environment with the TM.<sup>30</sup> A relevant difference is that Ni only has a divalent state so the conversion process can be isolated from the intercalation. Therefore, it is possible to directly explore the impact of O doping on the conversion process without forming the oxyfluoride phase. An additional encouraging feature is that the theoretical potential of conversion (2.96 V) is higher than the FeF<sub>x</sub> system, which may be more appropriate for the cathode materials.

In this study, we combine an in-depth analysis of XAS and PDF data to obtain comprehensive insights into the electrochemical reaction mechanism of NiO–NiF<sub>2</sub>–C electrodes. The effects of NiO doping and carbon composites on the conversion kinetics and reversibility are discussed by investigating the phases and size of Ni NPs in a discharged NiO–NiF<sub>2</sub>–C system. The structures and morphologies of the as-prepared materials were investigated by X-ray diffraction (XRD) and TEM. XAS measurements were conducted to study the conversion mechanisms and reversibility. To investigate the differences in the conversion reactions quantitatively, we analyzed the phases and Ni NPs size at the 1st and 2nd discharged states using extended X-ray absorption fine structure (EXAFS) and PDF. A better understanding of the NiF<sub>2</sub> based materials will help us obtain more concrete ideas on the conversion mechanism in TM–F<sub>x</sub> compounds.

## Experimental

### NiO–NiF<sub>2</sub>–C preparation

Commercially available NiF<sub>2</sub> (Alfa Aesar) powder was used for this study. Subsequently the NiF<sub>2</sub> was annealed at 500 °C for 1 hour under a mixture of argon and partial oxygen to dope the NiO phase. NiO–NiF<sub>2</sub>–C was prepared by high energy ball milling of NiO-doped NiF<sub>2</sub> with acetylene black (Strem Chemicals). Stoichiometric mixtures (NiF<sub>2</sub>: acetylene black = 80:20 wt%) were placed inside a planetary ball mill (PM 100, Retsch) and the milling was performed for 6 h at 500 rpm under an Ar atmosphere.

### X-ray diffraction (XRD)

XRD patterns were collected at ambient temperature on a Bruker D8 Advance diffractometer using a LynxEye detector at 40 kV, 40 mA using a Cu-anode (*K*α,  $\lambda = 1.5418$  Å), with a scan speed of 1 s per step, a step size of 0.02° in  $2\theta$ , and a  $2\theta$  range of 10–70°. XRD data analysis was carried out by utilizing Rietveld refinement using the FullProf software package.<sup>31</sup>

### Transmission electron microscopy (TEM)

The Sphera, a 200 KV instrument equipped with a LaB<sub>6</sub> electron gun, was utilized to investigate the morphology and structure of as-prepared NiO–NiF<sub>2</sub>–C material. Powder samples were hand-ground using a mortar and pestle, and dispersed in isopropanol using ultrasonication. A small amount of the solution was then dropped onto the carbon grids and then transferred into the TEM column. Micrographs were recorded on a 2K × 2K Gatan CCD camera.

### X-ray absorption spectroscopy (XAS)

X-ray absorption spectroscopy was carried out at beamline X11B of the National Synchrotron Light Source (NSLS) at Brookhaven National Laboratory. Customized coin cells were used to prevent the sample contamination. The electrode samples were never exposed to the ambient environment during the measurement. Higher harmonics in the X-ray beam were minimized by detuning the Si(111) monochromator by 40% at the Ni K-edge (8333 eV). Transmission spectra at the Ni K-edge were collected along with a simultaneous spectrum on a reference foil of metallic Ni to assure consistent energy calibration. Energy calibration was carried out by using the first derivatives in the spectra of Ni foil. Data were analyzed and refined using the Ifeffit<sup>32</sup> and Horae<sup>33</sup> packages.

### Pair distribution function (PDF) analysis

High-energy total X-ray scattering data ( $\lambda = 0.2128$  Å) were collected at the dedicated PDF beamline 11-ID-B at the Advanced Photon Source, Argonne National Laboratory. A large-area amorphous-silicon-based detector (Perkin-Elmer) was used to collect high values of momentum transfer ( $Q_{\max} \sim 18$  Å<sup>-1</sup>).<sup>34,35</sup> The raw images were integrated using the software FIT2d.<sup>36</sup> PDFgetX2<sup>37</sup> was used to correct the data for background contributions, Compton scattering and detector effects, and to Fourier transform the data to generate  $G(r)$ , the PDF. Structure models were refined against the PDF data within PDFgui.<sup>38</sup> The electrode samples were recovered at different states of charge by disassembling the coin cells inside

the glove box. The electrodes were washed with battery-grade DMC (Novolyte, packed and sealed in Kapton under an Ar atmosphere).

### Electrochemical characterization

Electrochemical characterization was performed using coin-type (2016) cells. The working electrodes were composed of NiO–NiF<sub>2</sub>–C, acetylene black and PVDF at a weight ratio of 70:20:10. For the pure NiF<sub>2</sub> electrodes, a 10:10:8 weight ratio of NiF<sub>2</sub>, acetylene black, and polyvinylidene fluoride (PVDF) were utilized. Pure lithium metal was used as a counter electrode and polypropylene C480 (Celgard) was used as a separator. The coin cells were assembled with the electrolyte consisting of 1 M LiPF<sub>6</sub> dissolved in ethylene carbonate (EC) and dimethylene carbonate (DMC) with a volume ratio of 1:1 (Novolyte) in an MBraun Ar-filled glove box (H<sub>2</sub>O < 0.1 ppm). Electrochemical cycling was performed using a battery cycler (Arbin) at room temperature, with a constant current density of C/20, and a cell potential range of 1.0–4.5 V.

## Results and discussion

### Properties of as-prepared NiO–NiF<sub>2</sub>–C material

The structures and morphologies of as-prepared NiO–NiF<sub>2</sub>–C were analyzed by XRD and TEM. XRD patterns of pure NiF<sub>2</sub> and NiO–NiF<sub>2</sub> were presented for comparison and are shown in Fig. 1(a). NiO was introduced into the NiF<sub>2</sub> as a second phase, observed at  $2\theta = 37^\circ$ ,  $43^\circ$  and  $63^\circ$ . The refinements by the Rietveld method were carried out and the refined parameters with reliability factors are presented in Table S1 (ESI<sup>†</sup>). Based on the refinement, it is estimated that  $\sim 14.6$  wt% of NiO was doped in the NiF<sub>2</sub> as a result of the annealing. The peaks corresponding to NiF<sub>2</sub> appeared to be sharper in NiO–NiF<sub>2</sub>, indicating that the crystallinity is improved by annealing. Decreased intensities and larger full width half maximum (FWHM) compared to the NiO–NiF<sub>2</sub> were shown in NiO–NiF<sub>2</sub>–C due to the nanosize peak broadening. A relatively high  $R_B$  factor was obtained in the refinement, which may be caused by the broadened XRD patterns. The reflections corresponding to the NiO phase were still observed as a second phase. Except for the peak broadening, no significant differences were observed in the lattice parameters and atomic positions in NiO–NiF<sub>2</sub>–C. The TEM image presented in Fig. 1(b) shows that nanosized NiF<sub>2</sub> was formed by lattice fringes spaced by 3.25 Å and 2.56 Å, which correspond to the distances of NiF<sub>2</sub>(110) and (101), respectively. The primary particle size of crystalline NiF<sub>2</sub> in NiO–NiF<sub>2</sub>–C was around 10–15 nm and they were surrounded by an amorphous carbon matrix ( $\sim 10$  nm in thickness), which possibly improves the electronic conductivity as well as protects the surface of the material.

### Electrochemical properties of NiO–NiF<sub>2</sub>–C electrodes

In this study, 4 different systems, pure NiF<sub>2</sub>, NiF<sub>2</sub>–C composite, NiO–NiF<sub>2</sub>, and NiO–NiF<sub>2</sub>–C, have been prepared and electrochemically evaluated (see Fig. S1, ESI<sup>†</sup>). Interestingly, NiO–NiF<sub>2</sub>–C showed the most enhanced cycling performances while

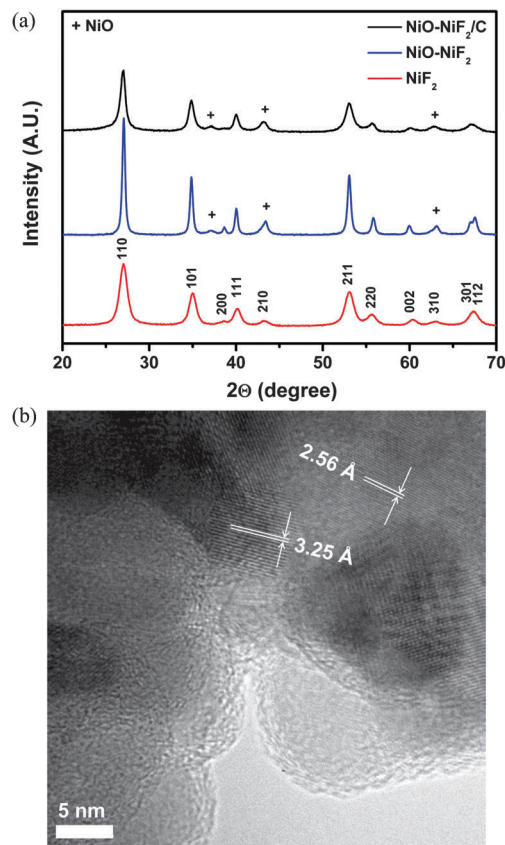


Fig. 1 (a) XRD patterns of NiO–NiF<sub>2</sub>–C (black), and pure NiF<sub>2</sub> (red) and NiO–NiF<sub>2</sub> (blue) for comparison. (*hkl*) marks the Bragg diffractions related to NiF<sub>2</sub>,  $P4_2/mnm$  and (+) indicates the NiO phase, and (b) TEM micrographs of as-prepared NiO–NiF<sub>2</sub>–C powder.

NiF<sub>2</sub>–C and NiO–NiF<sub>2</sub> exhibited only a slight improvement. Therefore, we more closely studied the two extreme cases, pure NiF<sub>2</sub> and NiO–NiF<sub>2</sub>–C, to understand the origin of different electrochemical behaviors. As shown in Fig. 2, the electrochemical properties of the NiO–NiF<sub>2</sub>–C electrode were investigated in the voltage range of 1.0–4.5 V at a C/20 rate. The NiF<sub>2</sub> electrode delivered 700 mA h g<sup>−1</sup> at the 1st discharge, which is around 150 mA h g<sup>−1</sup> greater capacity than the theoretical value due to the side reaction such as a solid electrolyte interphase (SEI) layer,<sup>3–5</sup> but the reversibility at the 1st charge was only 63.5% ± 1%. The capacity at the 1st discharge was lower in NiO–NiF<sub>2</sub>–C by around 15%, since 14–15 wt% of NiO was incorporated into NiF<sub>2</sub>. NiO can only be converted into Ni and Li<sub>2</sub>O under 0.5 V but remains inactive within the potential window used here.<sup>29</sup> The capacity with respect to the active NiF<sub>2</sub> component remained unchanged. Considerable improvement in the reversibility, 88% ± 1%, was obtained in NiO–NiF<sub>2</sub>–C upon the 1st cycle. The conversion potential was slightly increased by 0.15 V at the 1st discharge indicating that the overpotential was diminished. The large overpotential contains a significant component of polarization related to slow reaction kinetics particularly upon the lithiation (discharge) process.<sup>39</sup> As shown in Fig. S2 (ESI<sup>†</sup>), even higher conversion potential can be obtained at 70 °C. Based on the electrochemical properties,

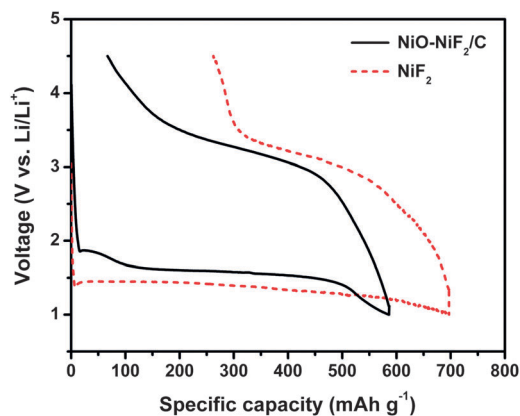


Fig. 2 The electrochemical profiles of 1st discharge and charge for NiO-NiF<sub>2</sub>-C and pure NiF<sub>2</sub> (red dots) with a C/20 rate in the voltage range of 1.0–4.5 V at room temperature. The theoretical capacity of NiF<sub>2</sub> is 550 mA h g<sup>-1</sup>.

it is suggested that the polarization during the 1st discharge is reduced possibly due to improved electronic conductivity by NiO (band gap: 4.3 eV)<sup>40</sup> doping into highly insulating NiF<sub>2</sub> (band gap: 6.5 eV)<sup>41</sup> and incorporation with conductive carbon.

### Conversion mechanisms and reversibility of NiF<sub>2</sub> and NiO-NiF<sub>2</sub>-C

To investigate the conversion mechanism and reversibility, XAS measurements including X-ray absorption near edge structure (XANES) and EXAFS were performed. As presented in Fig. 3(a), it is clearly observed that the magnitude of Ni<sup>2+</sup> absorption at around 8345 eV largely disappeared after the 1st discharge and shifted to lower energy corresponding to metallic Ni (8333 eV). This indicates that NiF<sub>2</sub> was converted to metallic Ni by the conversion process. The 1st derivative of XANES spectra in Fig. S3 (ESI<sup>†</sup>) provides a better indication of the shifts in edge energy. After the 1st charge of the NiF<sub>2</sub>, the XANES is consistent with the presence of both NiF<sub>2</sub> and metallic Ni, suggesting that the conversion process is partially reversible. Most of the re-converted NiF<sub>2</sub> was converted to metallic Ni by the 2nd discharge. Fundamentally, the same phenomena, which are partially reversible conversion processes, were observed in the NiO-NiF<sub>2</sub>-C electrode (see Fig. 3(b)); however, the spectra after the 1st charge display a larger portion of NiF<sub>2</sub> indicating that the reversibility of the conversion process is improved. It is also worth noting that the XANES spectra at the 1st and the 2nd discharge of NiO-NiF<sub>2</sub>-C were precisely overlapped suggesting that the reversibility beyond the 1st discharge is indeed good. The phase distribution of the electrodes at the different states of charge was estimated by linear combination fit to XANES using NiF<sub>2</sub>, NiO-NiF<sub>2</sub>-C and Ni foil references. The amount of conversion in the NiF<sub>2</sub> was around 94% at the 1st discharge, but only 47% of NiF<sub>2</sub> was regenerated after the 1st charge indicating poor reversibility. Considerably improved reversibility, around 80%, was shown in the NiO-NiF<sub>2</sub>-C electrode at the 1st charge, but still 20% of Ni was not re-converted into NiF<sub>2</sub> resulting in the irreversibility in the charging process. Most of the NiF<sub>2</sub>

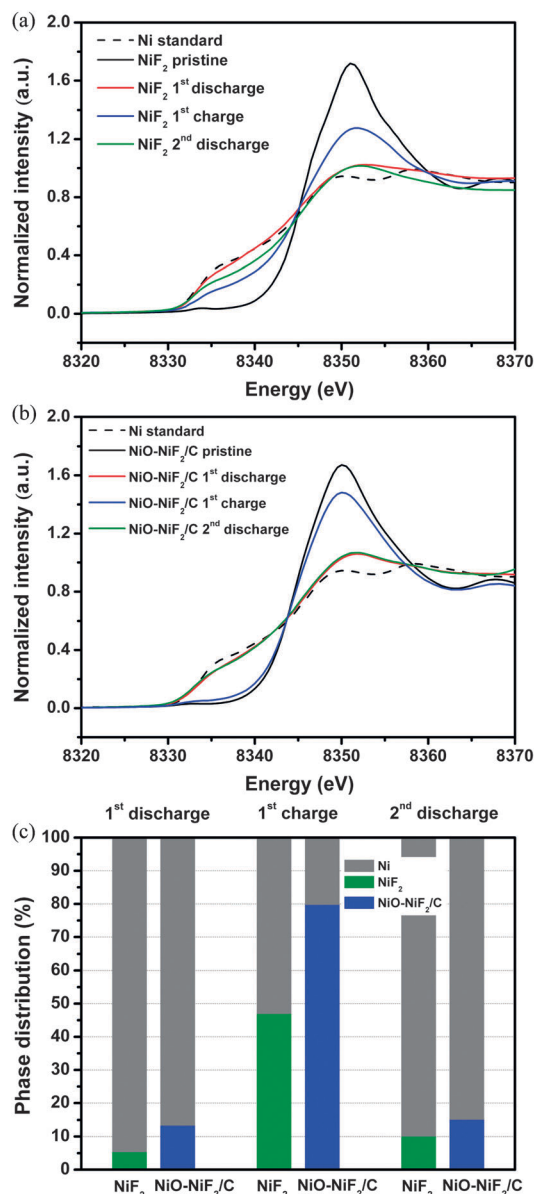


Fig. 3 XANES spectra at the Ni K-edge (8333 eV) of (a) NiF<sub>2</sub>, (b) NiO-NiF<sub>2</sub>-C at initial, 1st discharge, 1st charge and 2nd discharge including Ni metal standard (black dots), and (c) phase distribution at different states of charge by the linear combination fit.

was converted into Ni at the 2nd discharge in both electrodes. The XAS results including the amount of conversion and the reversibility are in good agreement with the electrochemical properties.

The EXAFS spectra of the NiF<sub>2</sub> and NiO-NiF<sub>2</sub>-C electrodes are shown in Fig. 4 and the refined structural parameters are summarized in Table 1. As shown in Fig. 4(a), the absence of the Ni-F contribution and the presence of the Ni-Ni contribution for the 1st discharged electrode are consistent with the reduction of Ni<sup>2+</sup> to metallic Ni. Although the amplitude of the Ni-F contribution was increased and the Ni-Ni contribution was reduced after the 1st charge in NiF<sub>2</sub>, both phases are still predominant indicating that the re-conversion process is not

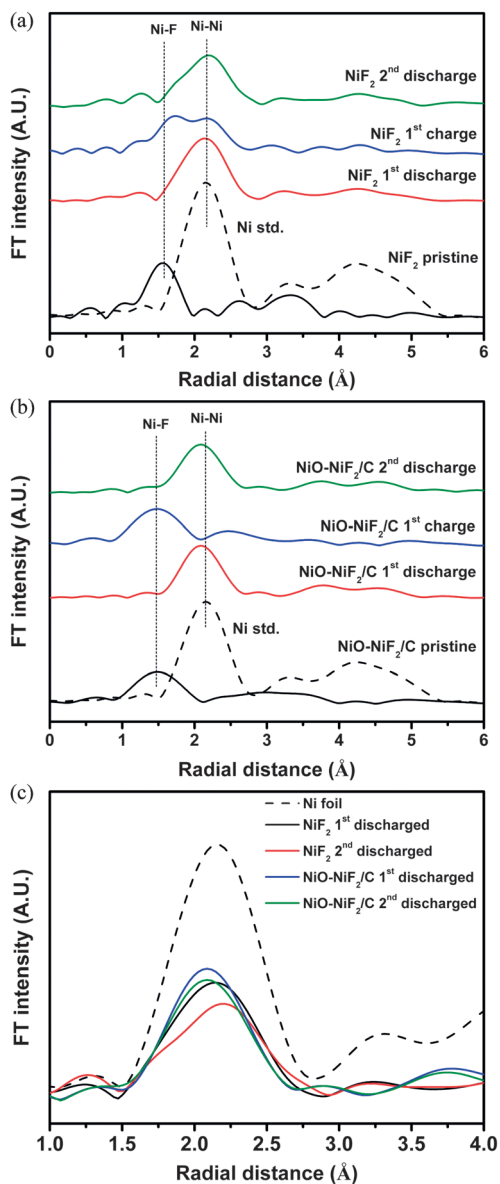


Fig. 4 EXAFS spectra at the Ni K-edge (8333 eV) of (a) NiF<sub>2</sub> at initial, 1st discharge, 1st charge and 2nd discharge including Ni metal standard (black dots), (b) NiO-NiF<sub>2</sub>-C at initial, 1st discharge, 1st charge and 2nd discharge including Ni metal standard (black dots), and (c) enlarged EXAFS regions for 1st and 2nd discharged electrodes along with Ni metal standard (black dots).

completely reversible. However, NiO-NiF<sub>2</sub>-C (see Fig. 4(b)) shows negligible Ni-Ni contribution in the 1st charged electrode, which means that the reversibility of the re-conversion is significantly improved. The pristine and the 1st charged NiO-NiF<sub>2</sub>-C exhibit very similar distance and intensity for the Ni-F bond suggesting that the changes in the Ni-F environment are very slight. Besides, both as-prepared and the 1st charged NiO-NiF<sub>2</sub>-C show relatively lower Ni-F amplitude than that of pure NiF<sub>2</sub> due to the nanosized NiF<sub>2</sub> in the composites. The lower amplitude of Ni-Ni of the 1st and 2nd discharged electrodes relative to that of Ni foil is consistent with formation of Ni NPs through the conversion process (see Fig. 4(c) and Fig. S4, ESI†). The magnitude of the

Fourier transformed (FT) intensity is diminished from the bulk Ni to Ni NPs, since the total amount of Ni-Ni coordination became smaller in NPs.<sup>42</sup> After the 2nd discharge, the intensity of Ni-Ni was further decreased in the NiF<sub>2</sub> electrode, however no noticeable differences were observed in the NiO-NiF<sub>2</sub>-C.

### Relationship between the conversion reaction and the particle size of Ni NPs

To elucidate the relationship between the conversion reaction kinetics and the size of Ni NPs, we compared the amplitude corresponding to Ni-Ni on the EXAFS spectra at each discharged state. It is clearly observed that the magnitude of Ni-Ni after the 1st discharge diminished in the NiF<sub>2</sub> compared to metallic Ni (see Fig. 4(c)) suggesting that Ni NPs were formed due to the slow growth rate of Ni upon the conversion process.<sup>16,43</sup> More quantitative studies on the size of Ni NPs were carried out by the refinement of structural models against the EXAFS data. The refined structural parameters including bond length, Debye-Waller factor ( $\sigma^2$ ), size of Ni NPs and *R*-factors are presented in Table 1. EXAFS is sensitive to crystallite size, since the average coordination number for a given scattering path is suppressed by a factor that depends upon the distance between the absorbing and scattering atoms.<sup>44</sup> In this sense, Calvin *et al.* suggested that the average particle size in the materials can be estimated by the following equation.

$$1 - \frac{3}{4}\left(\frac{r}{R}\right) + \frac{1}{16}\left(\frac{r}{R}\right)^3 \quad (1)$$

The crystallite is considered a homogeneous sphere of radius *R*. For multiple-scattering paths, *r* is the distance from the absorbing atom to the most distant scattering atom, rather than half of the total path length. On the basis of the EXAFS refinement, the average size of Ni NPs in the NiF<sub>2</sub> was approximately 3.29 nm after the 1st discharge and they became even smaller, 1.89 nm, after the 2nd discharge. It is worth noting that the bond distances of Ni-Ni in the 2nd discharged NiF<sub>2</sub> are slightly larger compared with the other discharged states. This type of lattice expansion can be ascribed to a nanosize effect, because similar expansions have also been detected in nanosized metals.<sup>21,45</sup> Nevertheless, the size of Ni NPs and the bond lengths appeared to be preserved until the 2nd discharge in NiO-NiF<sub>2</sub>-C electrode.

To evaluate the phase distribution and the Ni NPs size after the 1st and 2nd discharge, PDF measurements were carried out (see Fig. 5). The *r*-range over which well-defined features are evident in the PDF, *G*(*r*), reflects the length scale of well-ordered structural domains – no peaks are evident at distances beyond the size of the NPs.<sup>26</sup> A clear reduction in the length scale of ordering was evident from the PDFs for the cycled electrodes compared to pure NiF<sub>2</sub> systems. The PDFs for the 1st and 2nd discharged NiO-NiF<sub>2</sub>-C were very similar. The phase distributions and particle dimensions were quantified by refining structural models against the PDF data. This analysis shows that after the 1st discharge both systems consist of Ni NPs with a bimodal size distribution centered at ~14 Å and ~40 Å with a minor amount of rock salt NiO. During the 2nd discharge there

**Table 1** Refined structural parameters of the NiF<sub>2</sub> and NiO–NiF<sub>2</sub>–C at different discharge states obtained from EXAFS measurements at the Ni K-edge<sup>a</sup>

Sample	Phase	Atom	CN	<i>R</i> (Å)	$\sigma^2$ (10 <sup>-3</sup> Å <sup>2</sup> )	Ni particle size (nm)	<i>R</i> factor (%)
NiF <sub>2</sub> 1st discharged	Ni	Ni	12	2.478 ± 0.004	3.32 ± 0.02	3.29 ± 0.40	1.22
		Ni	6	3.506 ± 0.004	5.71 ± 0.10		
		Ni	24	4.294 ± 0.004	6.52 ± 0.09		
NiF <sub>2</sub> 2nd discharged	Ni	Ni	12	2.511 ± 0.019	3.24 ± 0.09	1.89 ± 0.33	1.01
		Ni	6	3.551 ± 0.019	9.63 ± 0.40		
		Ni	24	4.349 ± 0.019	8.41 ± 0.33		
NiO–NiF <sub>2</sub> –C 1st discharged	Ni	Ni	12	2.472 ± 0.010	2.60 ± 0.05	3.19 ± 0.43	0.73
		Ni	6	3.499 ± 0.010	3.72 ± 0.24		
		Ni	24	4.294 ± 0.010	9.14 ± 0.44		
NiO–NiF <sub>2</sub> –C 2nd discharged	Ni	Ni	12	2.471 ± 0.008	1.74 ± 0.04	2.88 ± 0.09	1.02
		Ni	6	3.494 ± 0.008	1.53 ± 0.02		
		Ni	24	4.279 ± 0.008	1.29 ± 0.19		

<sup>a</sup> The interatomic distance (*R*), Debye–Waller factor ( $\sigma^2$ ), and the size of Ni NPs was refined. The coordination number (CN) was fixed based on the structural model.

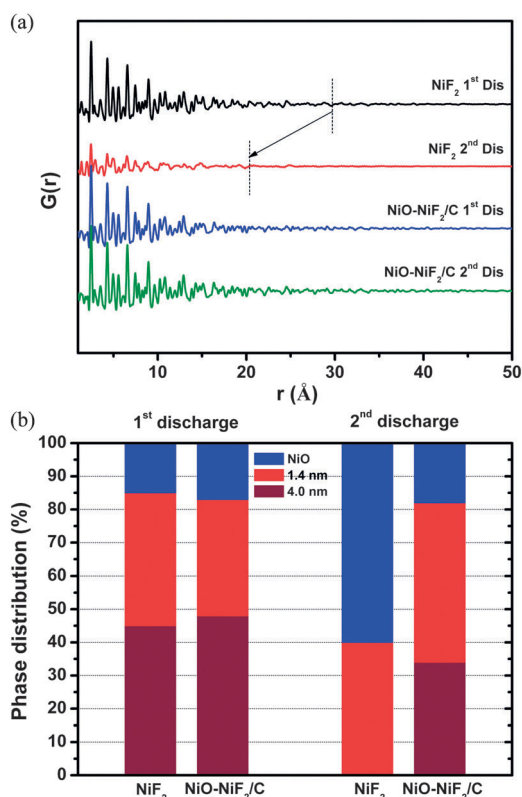


**Fig. 5** (a) Overall PDF profiles of the 1st and 2nd discharged NiF<sub>2</sub>, and NiO–NiF<sub>2</sub>–C, and (b) phase distribution by full profiles fits to the PDF data.

was a moderate (~10%) increase in the relative abundance of the smaller NPs for the NiO–NiF<sub>2</sub>–C system. This change in the NP size distribution likely reflects the decrease in the average NP size evident in the EXAFS analysis (31.9 Å to 28.8 Å) after the 2nd discharge (Table 1). By contrast, after the 2nd discharge for NiF<sub>2</sub>, as also evident in the EXAFS analysis, only the smaller NPs were observed.

The reduced Ni particle size following the 2nd discharge of the pure NiF<sub>2</sub> electrode can be attributed to slow kinetics of the

conversion process.<sup>29</sup> Since the conversion reaction starts from the surface and propagates inwards, the surface properties are pivotal to initiate the reaction.<sup>21</sup> Based on the observations by EXAFS and PDF, we suggest two plausible explanations here. First, an insulating SEI layer formed on the surface upon the 1st discharge possibly retards the re-conversion process, the growth of NiF<sub>2</sub>, resulting in smaller NiF<sub>2</sub> after the 1st charge. The Ni NPs formed from these smaller NiF<sub>2</sub> would likely be smaller than that formed from larger NiF<sub>2</sub>. Second, the growing SEI may interrupt the initiation of the reduction process (Ni<sup>2+</sup> to Ni<sup>0</sup>) on the surface of the NiF<sub>2</sub> upon the 2nd discharge. This limits the kinetics of the conversion process, the growth of Ni, resulting in even smaller NPs during the 2nd discharge. The refined phase fraction of NiO, which seems larger than expected in 2nd discharged NiF<sub>2</sub>, may be originated from a partial re-oxidation of Ni NPs during recovery of the electrode. It also cannot be ruled out that the LiF in the sample, which has a similar atomic structure to NiO, contributed to a certain portion of NiO since the conversion process produces a large quantity of LiF. In the NiO–NiF<sub>2</sub>–C, on the other hand, the NiO doping and the carbon layer surrounding the NiF<sub>2</sub> particles possibly provide enough electronic conductivity to initiate the conversion reaction on the surface, and may prevent the SEI from growing thicker. The enhanced conductivity on the surface maintains the kinetics of the conversion process until the 2nd cycle (see Fig. S7, ESI† for the schematic). Taking every observation and analysis into account, we deduce that the changes in size of Ni NPs for the 1st and 2nd discharged electrodes are affected by the electronic conductivity, specifically on the surface, and eventually correlated to the cyclability.

The NiO–NiF<sub>2</sub>–C system studied in this work provides an intriguing contrast to the FeOF–C system.<sup>27</sup> In FeOF, the O and F are disordered over the anion lattice sites of the rutile structure while O cannot be incorporated into rutile NiF<sub>2</sub>. Interestingly, at the end of the first cycle of FeOF, a two-phase mixture of rock salt (O-rich) and amorphous rutile (F-rich) co-exist in the form of a composite with the conductive carbon matrix. Our work is the first step to demonstrate that synthesis of a single phase

mixed anion system is unnecessary and the electrochemical performance enhancements in conversion systems may be realized by physical mixtures of oxides and fluorides. An appropriate nanostructuring of the composite remains to be optimized.

## Conclusions

The conversion mechanism of NiO–NiF<sub>2</sub>–C has been investigated and compared with pure NiF<sub>2</sub> using XAS and PDF analysis. The NiO–NiF<sub>2</sub>–C electrode showed a significantly improved reversible conversion reaction over pure NiF<sub>2</sub> due to enhanced electronic conductivity. It is observed by EXAFS that the average size of Ni NPs was diminished after the 2nd discharge in the pure NiF<sub>2</sub> electrode. The PDF analysis indicated that a bimodal size distribution (~14 Å and ~40 Å) of Ni NPs was found in both NiF<sub>2</sub> and NiO–NiF<sub>2</sub>–C electrodes after the 1st discharge. However, only smaller NPs (~14 Å) remained for pure NiF<sub>2</sub> after the 2nd discharge. This may be ascribed to poor electronic conductivity on the surface of the NiF<sub>2</sub> originated from a large amount of SEI layer formed upon the 1st discharge. In contrast, a bimodal size distribution was maintained for the NiO–NiF<sub>2</sub>–C since the NiO doping and the carbon layer on the surface possibly provide enough electronic conductivity to initialize the conversion reaction from the surface. Based on in-depth insights into the conversion mechanisms of NiF<sub>2</sub> and NiO–NiF<sub>2</sub>–C, we infer that the size changes in Ni NPs for the 1st and 2nd cycles are significantly influenced by the electronic conductivity; consequently have a strong correlation to the cyclability of the batteries.

## Acknowledgements

This material is based upon work supported as part of the Northeastern Center for Chemical Energy Storage (NECCES), an Energy Frontier Research Center (EFRC) funded by the U.S. Department of Energy, Office of Science, Office of Basic Energy Sciences under Award No. DE-SC 0001294. Work done at Argonne and use of the Advanced Photon Source, an Office of Science User Facility operated for the U.S. Department of Energy, Office of Science, by Argonne National Laboratory, were supported by the U.S. Department of Energy under Contract No. DE-AC02-06CH11357. XAS data for NiF<sub>2</sub> at the 1st charged and 1st discharged electrodes were collected by David Kwabi (MIT) and Dr Azzam Mansour (BNL) at NSLS beamline X11B. Use of the National Synchrotron Light Source, Brookhaven National Laboratory, was supported by the U.S. Department of Energy, Office of Science, Office of Basic Energy Sciences, under Contract No. DE-AC02-98CH10886. The authors acknowledge fruitful discussions with Prof. Glenn Amatucci.

## Notes and references

- J. Cabana, L. Monconduit, D. Larcher and M. R. Palacín, *Adv. Energy Mater.*, 2010, **22**, E170.
- M. Armand and J.-M. Tarascon, *Nature*, 2008, **451**, 652.
- P. Poizot, S. Laruelle, S. Grugeon, L. Dupont and J.-M. Tarascon, *Nature*, 2000, **407**, 496.
- A. Debart, L. Dupont, P. Poizot, J.-B. Leriche and J.-M. Tarascon, *J. Electrochem. Soc.*, 2001, **148**, A1266.
- P. Balaya, H. Li, L. Kienle and J. Maier, *Adv. Funct. Mater.*, 2003, **13**, 621.
- Y. Oumellal, A. Rougier, G. A. Nazri, J.-M. Tarascon and L. Aymard, *Nat. Mater.*, 2008, **7**, 916.
- P. Liao, B. L. MacDonald, R. A. Dunlap and J. R. Dahn, *Chem. Mater.*, 2008, **20**, 454.
- Z.-W. Fu, C.-L. Li, W.-Y. Liu, J. Ma, Y. Wang and Q.-Z. Qin, *J. Electrochem. Soc.*, 2005, **152**, E50.
- H. Li, G. Richter and J. Maier, *Adv. Mater.*, 2003, **15**, 736.
- H. Li, P. Balaya and J. Maier, *J. Electrochem. Soc.*, 2004, **151**, A1878.
- F. Badway, F. Cosandey, N. Pereira and G. G. Amatucci, *J. Electrochem. Soc.*, 2003, **150**, A1318.
- F. Badway, N. Pereira, F. Cosandey and G. G. Amatucci, *J. Electrochem. Soc.*, 2003, **150**, A1209.
- M. Bervas, F. Badway, L. C. Klein and G. G. Amatucci, *Electrochem. Solid-State Lett.*, 2005, **8**, A179.
- M. Bervas, A. N. Mansour, W.-S. Yoon, J. F. Al-Sharab, F. Badway, F. Cosandey, L. C. Klein and G. G. Amatucci, *J. Electrochem. Soc.*, 2006, **153**, A799.
- G. G. Amatucci and N. Pereira, *J. Fluorine Chem.*, 2007, **128**, 243.
- N. Yamakawa, M. Jiang and C. P. Grey, *Chem. Mater.*, 2009, **21**, 3162.
- I. D. Gocheva, I. Tanaka, T. Doi, S. Okada and J.-I. Yamaki, *Electrochem. Commun.*, 2009, **11**, 1583.
- N. Pereira, F. Badway, M. Wartelsky, S. Gunn and G. G. Amatucci, *J. Electrochem. Soc.*, 2009, **156**, A407.
- F. Badway, A. N. Mansour, N. Pereira, J. F. Al-Sharab, F. Cosandey, I. Plitz and G. G. Amatucci, *Chem. Mater.*, 2007, **19**, 4129.
- F. Wang, R. Robert, N. A. Chernova, N. Pereira, F. Omenya, F. Badway, X. Hua, M. Ruotolo, R. Zhang, L. Wu, V. Volkov, D. Su, B. Key, M. S. Whittingham, C. P. Grey, G. G. Amatucci, Y. Zhu and J. Graetz, *J. Am. Chem. Soc.*, 2011, **133**, 18828.
- F. Wang, H.-C. Yu, M.-H. Chen, L. Wu, N. Pereira, K. Thornton, A. V. d. Ven, Y. Zhu, G. G. Amatucci and J. Graetz, *Nat. Commun.*, 2012, **3**, 1201.
- N. Yamakawa, M. Jiang, B. Key and C. P. Grey, *J. Am. Chem. Soc.*, 2009, **131**, 10525.
- S. Rangan, R. Thorpe, R. A. Bartynski, M. Sina, F. Cosandey, O. Celik and D. D. T. Mastrogiovanni, *J. Phys. Chem. C*, 2012, **116**, 10498.
- B. Shyam, K. W. Chapman, M. Balasubramanian, R. J. Klingler, G. Srajer and P. J. Chupas, *Angew. Chem., Int. Ed.*, 2012, **51**, 4852.
- M. Newville, P. Livins, Y. Yacoby, J. J. Rehr and E. A. Stern, *Phys. Rev. B: Condens. Matter Mater. Phys.*, 1993, **47**, 14126.
- K. Page, T. Proffen, H. Terrones, M. Terrones, L. Lee, Y. Yan, S. Stemmer, R. Seshadri and A. K. Cheetham, *Chem. Phys. Lett.*, 2004, **393**, 385.
- K. M. Wiaderek, O. J. Borkiewicz, E. Castillo-Martínez, R. Robert, N. Pereira, G. G. Amatucci, C. P. Grey, P. J. Chupas and K. W. Chapman, *J. Am. Chem. Soc.*, 2013, **135**, 4070.
- H. Zhang, Y.-N. Zhou, Q. Sun and Z.-W. Fu, *Solid State Sci.*, 2008, **10**, 1166.

- 29 D. H. Lee, K. J. Carroll, S. Calvin, S. Jin and Y. S. Meng, *Electrochim. Acta*, 2012, **59**, 213.
- 30 W. H. Baur and A. A. Khan, *Acta Crystallogr., Sect. B: Struct. Crystallogr. Cryst. Chem.*, 1971, **27**, 2133.
- 31 J. Rodriguez-Carvajal, *Physica B*, 1993, **192**, 55.
- 32 M. Newville, *J. Synchrotron Radiat.*, 2001, **8**, 322.
- 33 B. Ravel and M. Newville, *J. Synchrotron Radiat.*, 2005, **12**, 537.
- 34 P. J. Chupas, K. W. Chapman and P. L. Lee, *J. Appl. Crystallogr.*, 2007, **40**, 463.
- 35 P. J. Chupas, X. Qiu, J. C. Hanson, P. L. Lee, C. P. Grey and S. J. L. Billinge, *J. Appl. Crystallogr.*, 2003, **36**, 1342.
- 36 A. P. Hammersley, S. O. Svensson, M. Hanfland, A. N. Fitch and D. Hausermann, *High Pressure Res.*, 1996, **14**, 235.
- 37 X. Qiu, J. W. Thompson and S. J. L. Billinge, *J. Appl. Crystallogr.*, 2004, **37**, 678.
- 38 C. L. Farrow, P. Juhas, J. W. Liu, D. Bryndin, E. S. Bozin, J. Bloch, T. Proffen and S. J. L. Billinge, *J. Phys.: Condens. Matter*, 2007, **19**, 1.
- 39 P. Liu, J. J. Vajo, J. S. Wang, W. Li and J. Liu, *J. Phys. Chem. C*, 2012, **116**, 6467.
- 40 G. A. Sawatzky and J. W. Allen, *Phys. Rev. Lett.*, 1984, **53**, 2339.
- 41 J. Zaanen, C. Westra and G. A. Sawatzky, *Phys. Rev. B: Condens. Matter Mater. Phys.*, 1986, **33**, 8060.
- 42 P. Zhang and T.-K. Sham, *Mater. Res. Soc. Symp. Proc.*, 2003, **738**, G13.14.11.
- 43 N. Yamakawa, M. Jiang, B. Key and C. P. Grey, *J. Am. Chem. Soc.*, 2009, **131**, 10525.
- 44 S. Calvin, C. Riedel, E. Carpenter, S. Morrison, R. Stroud and V. Harris, *Phys. Scr.*, 2005, **T115**, 744.
- 45 K. Lu and Y. H. Zhao, *Nanostruct. Mater.*, 1999, **12**, 559.